AIAA JOURNAL
Vol. 49, No. 10, October 2011

Overexpansion Effects on Characteristics of Mach Waves from a Supersonic Cold Jet

Taku Nonomura* and Kozo Fujii†
Japan Aerospace Exploration Agency, Sagamihara 229-8510, Japan

DOI: 10.2514/1.J051054

For predicting acoustic waves emitted from a rocket plume, the overexpansion effects on Mach 3.0 supersonic jet acoustics are investigated using an implicit large eddy simulation. A Mach 2.0 supersonic free jet is computed for code validation, and the results show qualitatively good agreement with the experiments. Then, computations of three different jets (design Mach numbers 3.0, 3.5, and 4.0 with fully expanded jet Mach number 3.0) are conducted, and nondimensionalizations based on design parameters and fully expanded parameters are discussed. Acoustic far-field spectra show that nondimensionalization based on fully expanded parameters works well for the high-Mach-number overexpanded jets, as it does for the low-Mach-number underexpanded jets that were investigated in previous studies. This nondimensionalization improves the accuracy of prediction of the acoustic waves emitted from rocket plumes because one parameter, the design Mach number, can be neglected for acoustic far fields. In addition, actual overexpansion effects after nondimensionalization are discussed. A comparison of the near flowfields and acoustic fields shows that Mach wave sources move upstream because of the existence of Mach disks, which enhances shear-layer mixing. Meanwhile, the overexpanded jet, which possesses only a shock cell without Mach disks, exhibits the same Mach wave generation characteristics as an ideally expanded jet.

Nomenclature

A	=	area of nozzle flow
a	=	sound speed
D	=	nozzle diameter
f	=	frequency
f_{AD}	=	function for area Mach number relation
L_{shock}	=	shock-cell length
M	=	Mach number
p	=	pressure
$\tilde{p}$	=	effective pressure fluctuation
R	=	distance from center of nozzle
Re	=	Reynolds number based on fully expanded condition
r	=	cylindrical coordinate
ref	=	reference value
SPL	=	sound pressure level
St	=	Strouhal number
T	=	temperature
TR	=	ratio of chamber temperature to ambient temperature
t	=	time
u	=	x-direction velocity
γ	=	specific heat ratio
θ	=	azimuthal angle
μ	=	coefficient of viscosity
ρ	=	density
φ	=	angle from axis

Subscripts

axis	=	value on axis
C	=	value for convection of disturbance
c	=	chamber condition
D	=	nozzle design (exit) condition
J	=	fully expanded condition
ref	=	value
th	=	throat condition
∞	=	ambient condition

Presented as Paper 2008-2836 at the 14th AIAA/CEAS Aeroacoustics Conference, Vancouver, 5–7 May 2008; received 5 November 2010; revision received 19 April 2011; accepted for publication 26 April 2011.

*Postdoctoral Fellow, Institute of Space and Astronautical Science, Department of Space Transportation Division, Kanagawa. Member AIAA.

†Professor, Institute of Space and Astronautical Science, Department of Space Transportation Division, Kanagawa. Fellow AIAA.

I. Introduction

IT IS understood that rocket plumes emit strong acoustic waves, particularly Mach waves. These waves are harmful to rocket payloads because these payloads are typically very light and have a fragile structure. Therefore, it is necessary to accurately predict acoustic waves and reduce their acoustic intensity level.

Several semiempirical methods are available for the prediction of acoustic waves emitted from a rocket plume [1,2]. These methods are based on experimental and actual launch data and have been used worldwide. However, the accuracy of the predictions obtained using these methods is unsatisfactory because of the limited knowledge of the detailed characteristics of acoustic wave emission, directivity, and sources. This is because of the difficulty of handling previous experimental data of rocket plumes.

Although practical simulations of acoustic waves emitted from rocket plumes have been conducted for predicting the acoustic environment in a limited low-frequency region, [3–5] improved prediction methods are also required for predicting the acoustic waves in a wider frequency region. To further improve the prediction accuracy, it is important to understand the characteristics of the Mach waves emitted from a rocket plume. In this study, a computational approach is adopted to understand the characteristics of Mach waves. A large eddy simulation (LES) is employed for computations because the results generated using LES agree well with the experimental results, and the data obtained using LES can yield a lot of valuable information about complex flowfields [6,7].

There are several parameter sets of a free supersonic jet, including the pressure ratio, the temperature ratio, and the design (nozzle exit) Mach number. It is important to choose suitable parameters from these sets to reduce the number of parameters used in the prediction model and yield more accurate predictions. Mach number, which is one of the nondimensional parameters, is discussed in this study for improving the prediction model.

Several researchers have reported that the sound pressure level (SPL) spectra of two different design Mach number M_D jets, both

with a constant ideally expanded Mach number M_J, are nearly the same under nondimensionalization [8–10]. This nondimensionalization works well for turbulent acoustic waves, but it does not work for shock-associated acoustic waves that are only emitted upstream in the case of underexpanded or overexpanded jets. In these studies, nondimensionalization is based on the fully expanded parameters (the fully expanded velocity u_J [11,12] or the diameter D_J) and not on the design (nozzle exit) parameters (nozzle-exit velocity u_D or diameter D). These parameters are defined in the next section.

The targets of this study are not the shock-associated acoustic waves emitted from a rocket plume; rather, they are the Mach waves, which are low-frequency waves that are strong in the downstream quadrant of jet, because they are critical for the payloads of rockets. Therefore, from the viewpoint of the prediction of acoustic waves emitted from a rocket plume, nondimensionalization based on ideally expanded parameters is effective, but nondimensionalization based on design parameters is not. Nondimensionalization based on the ideally expanded condition is a widely accepted technique and has been adopted in various studies of supersonic jets [13–16]; however, the parameters u_J and D are sometimes used for nondimensionalization as well. Although this nondimensionalization is verified with relatively low-Mach-number ($M_J \sim 2.0$) underexpanded jets [8–10], it has not been demonstrated whether this idea could be applied to high-Mach-number overexpanded jets such as rocket plumes.

Although there have not been any clear demonstrations of the effect of nondimensionalization based on the fully expanded condition of a rocket plume, this nondimensionalization has been applied to the prediction model of the acoustic waves emitted from a rocket plume. Varnier [2] proposed the use of the fully expanded parameters instead of the design parameters to predict the potential core length and to define the Strouhal number in the original prediction model [1] of acoustic waves from a high-Mach-number ($M_J \sim 3.0$) jet. The modified model shows better prediction accuracy for an experimental jet than the original one, and it is better to use fully expanded parameters instead of design parameters. However, it is not clear whether this modification is truly suitable because the modified model has other empirical parameters and it is difficult to verify all the assumptions in the modified prediction model. Therefore, it is important to validate the nondimensionalization for higher Mach number conditions.

Some researchers have demonstrated that the characteristics of far-field acoustic waves do not change under nondimensionalization based on the fully expanded condition for a relatively low-Mach-number jet [8–10]; however, the changes in flow and in the acoustic near fields have not been thoroughly investigated. For the prediction of acoustic waves emitted from a rocket plume, the position of the acoustic source is important because the SPL at the rocket fairing (which is near the rocket plume) is strongly affected by the source position. Therefore, changes in flow and changes in near-acoustic fields under nondimensionalization are also important for accurate prediction of acoustic waves from rocket plumes. Hereafter in this study, such changes observed under the nondimensionalization based on the fully expanded condition are called actual overexpansion effects.

For improving the prediction accuracy of acoustic waves from rocket plumes, it is necessary to verify the nondimensionalization based on fully expanded parameters and to understand actual overexpansion effects. In this study, the nondimensionalization based on the fully expanded parameters (u_J, D_J) is verified for high-Mach-number overexpanded jets by using LESs of ideally expanded and overexpanded jets. After verification of nondimensionalization, actual overexpansion effects on flow and near-acoustic fields are discussed.

In this study, supersonic cold jet conditions are adopted for studying these characteristics simply. In the next section, jet parameters and flow conditions are defined. In Sec. III, the numerical methods adopted in this study are presented. In Sec. IV, the results of code validation are discussed. In Sec. V, nondimensionalization based on the fully expanded parameters is verified and the actual overexpansion effects are discussed by simulating supersonic jets with varying M_D and constant M_J. Finally, Sec. VI concludes the paper.

II. Jet Parameters and Flow Condition

To verify our approach of nondimensionalization based on the fully expanded parameters and to investigate the actual overexpansion effects, four parameters are chosen to represent the jet conditions. These are the fully expanded Mach number M_J, the Mach design number M_D, the temperature ratio TR, and the Reynolds number Re. Here, M_J denotes the Mach number when the gas present in the chamber is ideally expanded and M_D denotes the Mach number at the nozzle condition, which is determined by the ratio of the cross-sectional area of the throat to that of the nozzle exit. These parameters are calculated using quasi one-dimensional isentropic flow equations as follows:

$$M_J = \frac{u_J}{a_J} = \sqrt{\frac{2}{\gamma - 1}\left(\left(\frac{p_c}{p_\infty}\right)^{(\gamma-1)/\gamma} - 1\right)} \tag{1}$$

$$M_D = \frac{u_D}{a_D} = f_{AD}\left(\frac{A_D}{A_{\text{th}}}\right) \tag{2}$$

$$TR = \frac{T_c}{T_\infty} \tag{3}$$

$$Re = \frac{\rho_J D_J u_J}{\mu_J} \tag{4}$$

where

$$D_J = \left(\frac{1 + 0.5(\gamma - 1)M_J^2}{1 + 0.5(\gamma - 1)M_D^2}\right)^{(\gamma+1)/(4\gamma-1)} \sqrt{\frac{M_D}{M_J}} D \tag{5}$$

Here, u, a, A, T, p, γ, and ρ are the velocity, speed of sound, area of nozzle flow, temperature, pressure, ratio of specific heat, and density, respectively. Function f_{AD} presents the relation between Mach number and area of flow [17]. Subscripts c, th, J, and D denote the chamber condition, the throat condition, the fully expanded condition, and the nozzle-exit condition, respectively. These quantities can be computed by substituting the Mach number in the quasi one-dimensional isentropic flow equations. Air is assumed to be the working fluid, and γ is set to 1.4.

In this study, overexpansion effects are investigated by simulating both the ideally expanded and overexpanded jets. Thus, M_D is equal to or greater than M_J. First, a case where $M_D = 2.0$ and $M_J = 2.0$ is simulated in order to validate the computational code. For the detailed discussion of overexpansion effects on Mach waves, three cases with $M_D = 3.0$, 3.5, and 4.0 while keeping $M_J = 3.0$ are analyzed. In total, four cases are discussed. These cases are referred to as $MJ(M_J \times 10)MD(M_D \times 10)$. For example, MJ30MD30 represents the case with $M_J = 3.0$ and $M_D = 3.0$ for an ideally expanded jet. The jet parameters for each simulation are given in Table 1, and the details of jet conditions are shown in Table 2. Parallel flow with a top-hat profile is assumed for jet inflow.

For all the cases investigated in this study, Re is set to 1.8×10^5 (for MJ20MD20) or 3.0×10^5 (for other cases), and TR is set to 1. Although these conditions are much different from rocket plume conditions, they are chosen to improve computational efficiency and

Table 1 Jet parameters

	M_J	M_D	Re	TR
MJ20MD20	2.0	2.0	180,000	1.0
MJ30MD30	3.0	3.0	300,000	1.0
MJ30MD35	3.0	3.5	300,000	1.0
MJ30MD40	3.0	4.0	300,000	1.0

Table 2 Detailed jet conditions

	ρ_J/ρ_∞	u_J/a_∞	p_J/p_∞	D/D_J	ρ_D/ρ_∞	u_D/a_∞	p_D/p_∞
MJ20MD20	1.800	1.491	1.000	1.000	1.800	1.491	1.000
MJ30MD30	2.800	1.793	1.000	1.000	2.800	1.793	1.000
MJ30MD35	2.800	1.793	1.000	1.266	1.348	2.092	0.482
MJ30MD40	2.800	1.793	1.000	1.591	0.677	2.390	0.242

to more easily understand the overexpansion effects on Mach waves. Therefore, the quantitative discussion should be carefully conducted as the quantity of the potential core length that is sensitive to Re and TR [18].

A top-hat profile type is used for the jet inflow boundary discussed earlier, while a 1/7 law is adopted for the boundary layer near the jet boundary region. The thickness of the boundary layer is set to $0.05D_J$. The boundary layer is thin compared with the grid spacing at the nozzle lip discussed later, and the flowfields near the nozzle lip are underresolved in our simulation. However, the validation result discussed later shows that such a treatment does not strongly matter for qualitative discussion of a Mach wave emission caused by a large-scale turbulence structure. Also, no disturbance is used in the jet flow condition. In general, a disturbance is required to eliminate spurious axisymmetric modes in a high-subsonic jet computation [19,20]. However, a supersonic shear layer does not seem to require such a disturbance because, unlike a high-subsonic jet, three-dimensional instability is inherently stronger than axisymmetric instability [21,22]. This thin shear layer easily excites three-dimensional instability without any numerical disturbances. Also, the no-disturbance condition is intentionally chosen for fair comparison of different cases because it is very difficult to add the same instability wave to the ideally expanded and overexpanded jets.

In addition, St_D, St_J, and SPL, which are used in Sec. IV, are defined as follows:

$$St_J = \frac{fD_J}{u_J} \tag{6}$$

$$St_D = \frac{fD}{u_D} \tag{7}$$

$$\mathrm{SPL} = 20\log_{10}\frac{\tilde{p}}{\tilde{p}_{\mathrm{ref}}} \tag{8}$$

where $\tilde{p}_{\mathrm{ref}}$ is defined as follows:

$$\tilde{p}_{\mathrm{ref}} = \frac{2.0\times10^{-5}\ \mathrm{Pa}}{101,300\ \mathrm{Pa}}\times p_\infty \tag{9}$$

III. Numerical Approach

A. Numerical Methods

Three-dimensional compressible Navier–Stokes equations that are nondimensionalized using the speed of sound under ambient conditions and fully expanded nozzle diameter D_J are computed as the governing equation. Hereafter, all the variables and computational grids are normalized based on the speed of sound under ambient conditions and fully expanded nozzle diameter D_J unless otherwise noted.

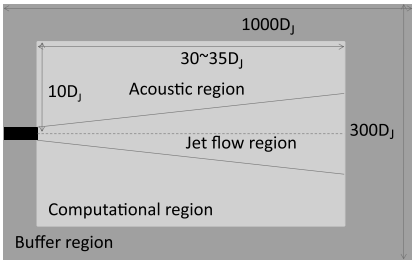

Fig. 1 Computational domain.

A seventh-order modified weighted compact nonlinear scheme (WCNS) is employed as the advection term. WCNS is a shock-capturing high-order scheme that was developed as a combination of the weighted essentially nonoscillatory scheme (WENO) [23] and compact schemes [24] by Deng and Zhang [25]. Compared with WENO, WCNS has a higher resolution [25,26], the capacity to handle various flux functions [25], and freestream preservation [27,28]. Both seventh- and ninth-order WCNSs have been developed by Nonomura et al. [29] and Zhang et al. [26] independently. In the seventh-order WCNS, a seventh-order upwind WENO-like node-to-midpoint interpolation scheme and an eighth-order explicit midpoint-to-node difference scheme [30] are used.

For improving the efficiency of WCNS, two modifications have been adopted. For improving the resolution, a relative limiter [31,32] is used as a smoothness indicator. For reducing the computational cost, nonlinear computations are localized in the nonsmooth flow region [32]. Special treatment for metrics proposed by Nonomura et al. is adopted to preserve a geometric conservation law [27]. For the flux function in the WCNS code, a simple high-resolution upwind scheme (SHUS) [33] is adopted. SHUS is a robust, high-resolution, and computationally cheap advection upwind splitting method (AUSM) [34] type of flux function.

With regard to the viscosity term, a sixth-order central difference scheme is used. With regard to turbulent modeling, a monotonically integrated LES (MILES) [35] approach is adopted using an upwind scheme. Therefore, no explicit LES subgrid-scale models are used. Recently, a similar MILES approach using WCNS has been validated [36,37] for basic turbulent flows. With regard to the time integration, a third-order total variation diminishing Runge–Kutta scheme [38] is used.

With regard to boundary conditions, the nonslip wall condition is imposed on the nozzle surface and the simple outflow condition is used for far fields. This outflow condition is not a nonreflection boundary condition, but no significant reflection is observed. This is because we use a very large damping region based on grid stretching [18].

B. Computational Domain, Grids, and Time Stepping

The computational domain is shown in Fig. 1. The computational domain consists of a computational region and a buffer region, where the length of the computational domain is based on the fully expanded diameter. The grid-scale flow and acoustic fields are solved within the computational region, while the flow and acoustic waves are damped using grid stretching in the buffer region [39]. The lengths of each computational region for each computational case are presented in Table 3.

The computational grids are shown in Figs. 2 and 3. The computational grids are axisymmetric at $r > 0.3D_J$. Square grid types are employed near the axis region at $r < 0.25D_J$ (Fig. 3). This type of grid is used for avoiding severe restriction in Δt using a purely axisymmetric grid because of the very small spacing near the axis. Grid type is gradually changed from axisymmetric to square, and the whole computational grid is divided into seven zones that are suitable

Table 3 Computational domain for each case

	Computational domain
MJ20MD20	$0 < x/D_J < 30, 0 < r/D_J < 10$
MJ30MD30	$0 < x/D_J < 35, 0 < r/D_J < 10$
MJ30MD35	$0 < x/D_J < 35, 0 < r/D_J < 10$
MJ30MD40	$0 < x/D_J < 35, 0 < r/D_J < 10$

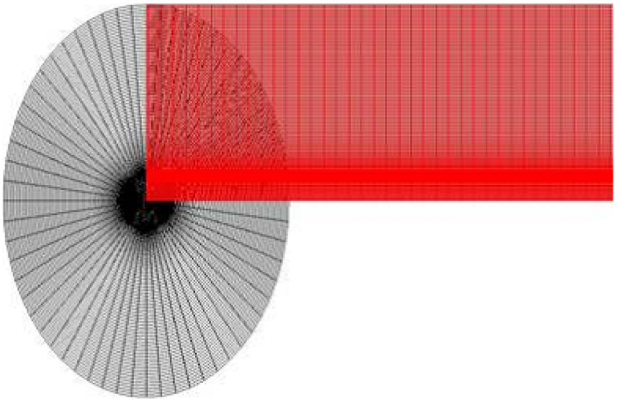

Fig. 2 Computational grids within computational region.

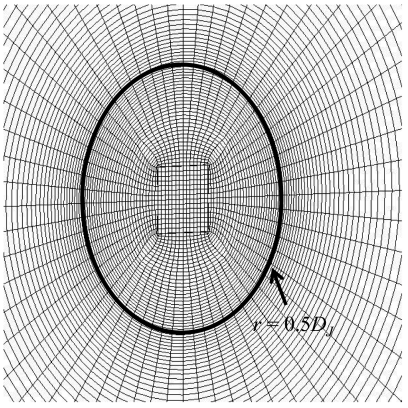

Fig. 3 Zoomed computational grids within computational region.

to our in-house computational codes. Axial, azimuthal, and radial grid points are set to 935–1085, 60, and 224, respectively. The total number of grid points is approximately 10–12 million. The grid points for each computational case are shown in Table 4.

The minimum grid spacing, which is the same for each case, is $0.033D_J$, $0.02D_J$, and $0.01D_J$ in the axial, azimuthal, and radial directions, respectively. The grid spacing at the nozzle lip is $0.033D_J$, $0.05D_J$, and $0.01D_J$ in the axial, azimuthal, and radial directions, respectively. In the axial and azimuthal directions, equal grid spacing is employed. In the radial direction, the maximum grid spacing is $0.05D_J$ and $0.1D_J$ in the jet flow region and in the acoustic wave propagating region. From the grid spacing in the acoustic wave propagating region, the cutoff Strouhal number for acoustic waves is estimated as 1.0, assuming that eight points per wave are required for the present scheme. Although these grid points are not sufficient for an accurate LES, the present grid points are sufficient to resolve the emission and propagation of low-frequency Mach waves, as discussed later.

The time-stepping interval Δt is set to $0.003D_J/a_\infty$–$0.005D_J/a_\infty$, and the resulting Courant–Friedrichs–Lewy number is approximately set to 1.0. The time steps and the total number of time steps for each case are shown in Table 4.

Table 4 Approximate grid numbers and time steps for each case[a]

	Approximate grid number ($x \times \theta \times r$)	Time-stepping interval	Number of time steps
MJ20MD20	$935 \times 60 \times 224$	0.005	40,000
MJ30MD30	$1085 \times 60 \times 224$	0.003	80,000
MJ30MD35	$1085 \times 60 \times 224$	0.003	80,000
MJ30MD40	$1085 \times 60 \times 224$	0.003	80,000

[a] Here, the computed time steps do not include those of the early stage of computation, which are not quasi steady.

C. Postprocessing

The three-dimensional computation begins with the axisymmetric results that are previously computed, and the computation is conducted until $t = 100D_J/a_\infty$ to get quasi-steady state. Then, the computations are continued and the data begin to be obtained. The time steps presented in Table 4 do not include the early computation before $t = 100D_J/a_\infty$. For processing data, temporal and azimuthal averaging are employed. Temporal averaging is conducted for the duration $200D_J/a_\infty$ for MJ20MD20, or for the duration $240D_J/a_\infty$ for other cases. Azimuthal averaging is conducted for 12 equally different plane data.

Next, an estimation of SPL is described. In the computational region, the pressure history is stored and used for estimating the SPL directly. A discrete Fourier transformation (DFT) is conducted with a fast Fourier transformation algorithm in order to compute the spectrum of the SPL data. Since the data are averaged between 12 azimuthal points, errors in DFT analysis are reduced. In addition, the cutoff frequencies are determined; for the low cutoff frequency, the frequency corresponding to the 10th mode in the DFT is used for obtaining a reliable SPL [18], while the high cutoff frequency is determined based on the resolution of the scheme and the maximum grid spacing. In this problem, eight points per wave are assumed for the computational scheme as discussed before. Resulting low and high cutoff Strouhal numbers are 0.05 and 1.0, respectively. Data outside these cutoff frequencies are shaded in the spectra provided after. For the SPLs from mid to far field, the frequency domain Kirchhoff method [40] is employed. The integral surface is set to $r = 10D_J$ at $0 < x/D_J < 30$ for MJ20MD20 and $r = 10D_J$ at $0 < x/D_J < 35$ for $M_J = 3.0$ cases. For the microphone array method used in Sec. V, the midfield sound pressure signal is computed using the time-domain Kirchhoff method [40], while the integral surface is the same as that for the frequency domain Kirchhoff method.

IV. Validation of the Computational Code

Code validation is conducted for understanding the errors in the present computations. Well-known experimental data [41–44] of similar ideally expanded jet conditions are used. The jet parameters adopted in these studies are summarized in Table 5.

First, the instantaneous flowfield (Fig. 4) is discussed qualitatively. The potential core, developed region, and mixing region of a jet can be seen. Also, Mach waves from the jet are observed as depicted.

Next, we present a quantitative analysis. The Mach number distributions along the jet axis are shown in Fig. 5. The position of the potential core end of the present study is approximately estimated to be $7D_J$, where those in experimental jets are estimated to be $9.5D_J$ for Troutt and McLaughlin's data [43] and $D_J = 12.5$ for Seiner and Ponton's data [42]. Here, the potential core length is defined as the position of $M_{\text{axis}}/M_J = 0.95$ and $\partial M_{\text{axis}}/\partial x < 0$ in this study, where M_{axis} is the averaged Mach number on the axis. The present potential core length is relatively close to that of the similar Reynolds number experiment, but it is still shorter for quantitative comparison. This difference in the potential core length is due to the difference in the Reynolds number, the shear-layer thickness at nozzle exit, and/or the nozzle contour. The potential core end of Seiner and Ponton's data of an experimental jet with a higher Reynolds number is observed further downstream. The results show that it is difficult to quantitatively predict the potential core length of rocket plumes, which have a very high Reynolds number compared with our simulation. Also, it is difficult to directly simulate high-Reynolds-number rocket

Table 5 Experimental and computational parameters used in the validation studies, where all referred data are experimental

Authors	M_J	M_D	Re	TR_C	U_J/a_∞
Lau et al [41]	1.37	1.37	630,000	1.38	1.37
Seiner and Ponton [42]	2.0	2.0	5,600,000	1	1.49
Troutt and McLaughlin [43]	2.1	2.1	70,000	1	1.53
Tanna [44]	1.95	1.95	660,000	1	1.47
Present study	2.0	2.0	180,000	1	1.49

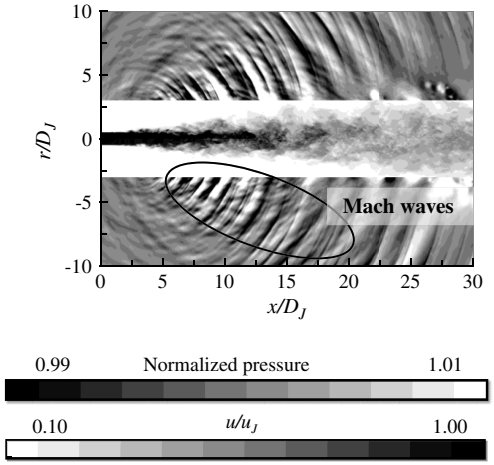

Fig. 4 Instantaneous flow and acoustic fields of MJ20MD20. The central region shows the velocity field, and the outer region shows the acoustic pressure field. For the velocity fields, contours are set from $0.1u_J$ to u_J. For pressure fluctuations, contours are set from $-0.01P_\infty$ to $0.01P_\infty$.

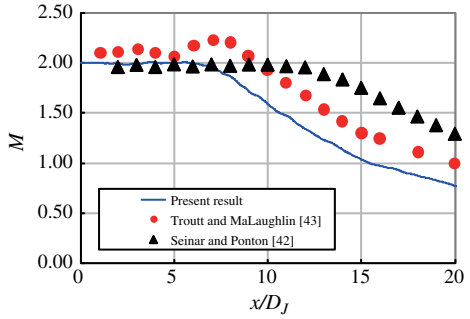

Fig. 5 Comparison of the distribution of the Mach number along the jet axis.

plumes because of high computational cost. However, qualitative discussion of jet Mach number and temperature on the potential core length seems to be available if the same computational settings (nozzle-exit condition, Reynolds number, and grid resolutions) are adopted, because qualitative characteristics of the potential core are captured in simulations with changing jet Mach number and temperature in [18].

Then, the velocity and velocity fluctuations are compared with another experimental result that has velocity fluctuation data where the jet condition is slightly different. A comparison of the axial velocity distribution with another experimental result (Fig. 6) shows good agreement. Here, u_J/a_∞ and the Reynolds number of the experimental condition are almost the same as they are in the present study, while the jet Mach number of the experimental condition is different. Root mean square of velocity fluctuations are shown in Fig. 7, where u' in Fig. 7 denotes the fluctuation of the velocity. This figure also illustrates that the positions of the peak velocity fluctuations and their peak values are almost equal, while the present

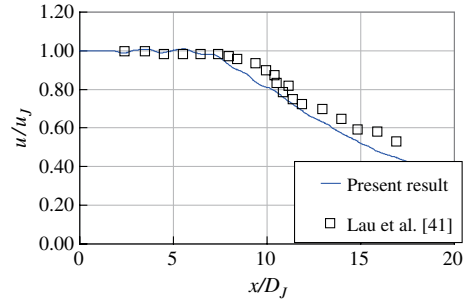

Fig. 6 Comparison of the velocity distribution along the jet axis.

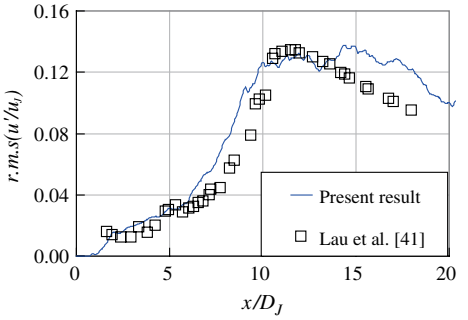

Fig. 7 Comparison of velocity fluctuation distribution along the jet axis.

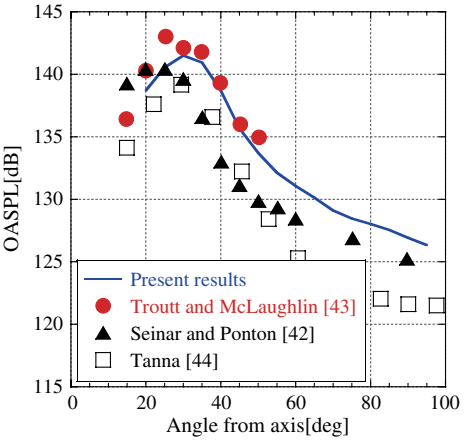

Fig. 8 Comparison of directivity. Here, the distance from the origin point is reset to $R = 40D_J$ by using the $1/R$ law.

results have a slightly higher value at $x/D_J > 10$. This result shows that the turbulence fluctuation of the jet is reasonably resolved in our simulation.

The midfield directivities of acoustic waves at $R = 40D_J$, shown in Fig. 8, illustrate that the present computational results show agreement with those of the experimental data of $M_J = 1.95$–2.1 with an error of 2–5 dB, where R denotes the distance from the center of the nozzle. The present computational results show excellent agreement with Troutt and McLaughlin's data (an experimental jet with almost the same Reynolds number) [43], which is a good outcome toward the objective of the present study. It is true that the peak angle of SPL for the experimental data with a higher Reynolds number is much lower than in this study; this may be due to differences in Reynolds number, inflow condition, and nozzle contour.

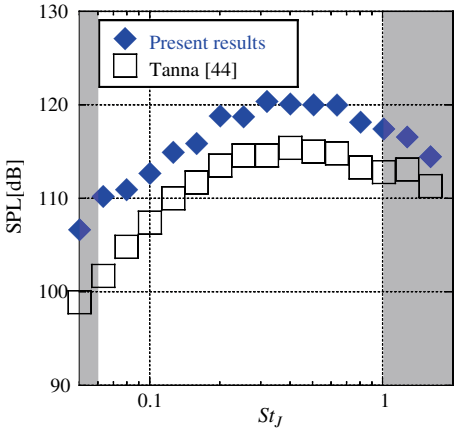

Fig. 9 Comparison of one-third OBSPL.

Finally, the one-third octave-band spectra at $R/D_J = 70$, $\varphi = 45$ deg compared with Tanna's data is shown in Fig. 9 [44], where φ denotes the angle from the axis. Although our computational result overpredicts the SPL by approximately 5 dB, the overall shape of the plot of the present computation is almost the same as that of experimental data within the cutoff frequencies. This qualitative correspondence is sufficient for a qualitative discussion of Mach wave emissions. The overprediction of our computational results corresponds to the fact that the experimental data with a higher Reynolds number have a lower peak angle of directivity, as discussed using Fig. 8. Therefore, this quantitative overprediction might be due to the difference in jet conditions. Finally, it should be noted that we have previously discussed the details of our validation results for velocity, velocity fluctuation, directivity, and spectra [18].

V. Investigation of Overexpansion Effects on M_J 3.0 Jets

In this section, effects of nondimensionalization based on fully expanded parameters are discussed using acoustic far fields of three jets. Then, the differences in flow and acoustic fields of three jets caused by actual overexpansion effects are discussed under this nondimensionalization.

A. Verification of Nondimensionalization Based on Acoustic Far-Field Data

The far-field acoustic spectra of MJ30MD30, MJ30MD35, and MJ30MD40 are shown in Figs. 10 and 11. Here, Fig. 10 shows the spectra at $R/D = 100$ with nondimensionalization based on the nozzle-exit condition (u_D, D, St_D) and Fig. 11 shows the spectra at $R/D_J = 100$ with nondimensionalization based on the fully expanded condition (u_J, D_J, St_J). The spectra nondimensionalized by the nozzle-exit condition (Fig. 10) do not agree with each other, and a difference of nearly 10 dB around $St_D = 0.05 \sim 0.5$ is observed. On the other hand, the spectra nondimensionalized by the fully expanded condition (Fig. 11) show very good agreement with an error of 5 dB or less. Thus, the better collapse of data is observed by the nondimensionalization based on the fully expanded condition rather than on that based on the nozzle-exit condition.

This result indicates that nondimensionalization based on the fully expanded parameters [8–10] is applicable to $M_J \sim 3.0$ overexpanded jets, which simulate the rocket plume conditions except for the Reynolds number and temperature condition. This knowledge is very important to build a new prediction model for acoustic waves from a rocket plume because we can reduce one jet parameter, M_D, to predict Mach wave emission while improving the prediction accuracy by using fully expanded parameters.

Given the results discussed above, only the nondimensionalization based on the fully expanded condition is used for the discussion of actual overexpansion effects of these three jets in the rest of this paper.

Figure 11c shows that spectra at 90 deg of MJ30MD30 has a higher SPL than that of the ideally expanded jet from $St_J \sim 0.2$ to 0.5 while its peak position is $St_J \sim 0.25$. These high SPLs in spectra are due to the shock-associated acoustic waves, which are caused by the interaction between the shear-layer fluctuation and the shock cells in

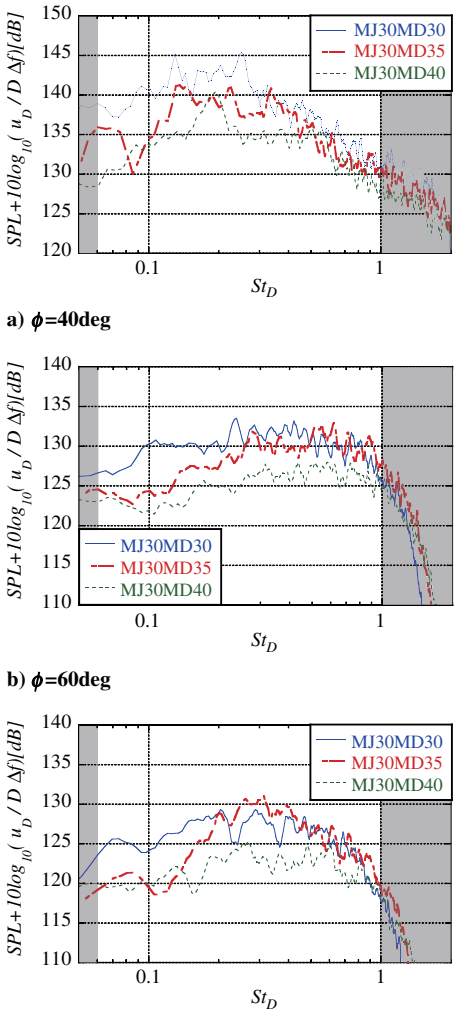

Fig. 10 Far-field SPL at $100D$ for $M_J = 3.0$ jets. Here, SPL is nondimensionalized by the nozzle-exit velocity u_D and width D.

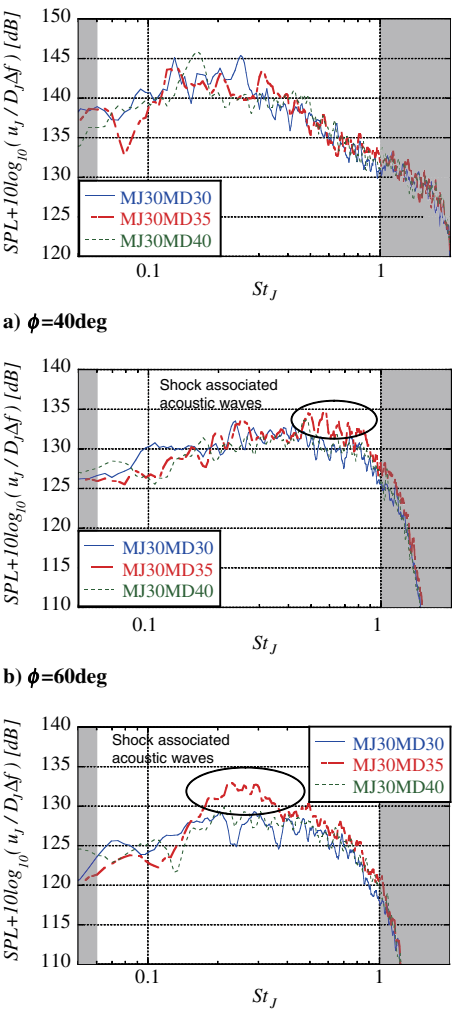

Fig. 11 Far-field SPL at $100D_J$ for $M_J = 3.0$ jets. Here, SPL is nondimensionalized by the fully expanded velocity u_J and width D_J.

the overexpanded jet. Based on the theoretical prediction of shock-associated acoustic waves in [45], the Strouhal number $St_{J,SA}$ of the primary mode of shock-associated acoustic waves propagating to the angle of 90 deg from the axis is written as

$$St_{J,SA} = \frac{U_C}{L_{\text{shock}}}\frac{D_J}{U_J} \tag{10}$$

where U_c is the convective velocity of disturbance and L_{shock} is the shock-cell length. The peak frequency of the shock-associated acoustic waves of MJ30MD35 at the angle of 90 deg is compared with this formula. In the present study, $U_C = 0.8U_J$; that is, the experimentally and theoretically obtained value is used, where this approximation works well for estimation of the Mach wave emission angle discussed later. Also, $L_{\text{shock}} = 2.6D_J$ is used, which is measured from computational results. Based on these parameters, $St_{J,SA}$ is estimated to be 0.30, which is near the present result. From this comparison, these higher SPL can be identified as shock-associated acoustic waves. On the other hand, spectra at 90 deg of MJ30MD40 do not have strong shock-associated acoustic waves. As discussed in [46], the shock-associated acoustic waves become stronger as the condition goes far from the ideal condition before Mach disk forms and it becomes weaker as the condition goes far from the ideal condition after Mach disk forms. In the case of MJ30MD40, in which the Mach disk is stably formed, shock-associated acoustic waves should be smaller than the condition when the Mach disk begins to form. However, we are not sure why the shock-associated acoustic waves are very weak for this case. It is probably due to the inflow condition.

The shock-associated acoustic waves are observed only in the upstream region, because the Mach waves, which are stronger than shock-associated acoustic waves, are more dominant in the downstream region. This is the primary difference between ideally expanded and overexpanded jets in far-field spectra. The shock-associated acoustic waves will not be discussed since the focus of this study is on Mach wave emission.

Figure 12 shows the directivity of the SPL estimates. Overexpanded jets have a slightly lower peak angle of directivity and a slightly higher SPL at large angles ($\varphi > 60$ deg) as compared with ideally expanded jets. The shift in the peak angle of directivity might result from the difference in Mach wave emissions that is caused by the difference in the convective velocity of disturbance, which is a Mach wave source. The computed angle of maximum Mach wave emission is 43 deg for MJ30MD30, 40 deg for MJ30MD35, and 38 deg for MJ30MD40. Based on these Mach wave angles, estimated convective velocities are $U_C/U_J = 0.79$ for MJ30MD30, $U_C/U_J = 0.75$ for MJ30MD35, and $U_C/U_J = 0.73$ for MJ30MD40. The convection velocity of MJ30MD30 is in good agreement with the empirical estimation of $U_C = 0.8U_J$, which corresponds to 44 deg of Mach wave emission. Here, this estimation ($U_C = 0.8U_J$) was experimentally obtained in [43] and works well for the prediction of Mach wave angles for various jets [47]. A slight difference in the convective velocities of disturbance for ideally expanded and overexpanded jets might be due to an increase in the entropy in the vicinity of the shock waves around the overexpanded jets. This is because the effective fully expanded Mach number is changed due to increase in the entropy (decrease in the total temperature). However, note that the difference in SPL at low angles is small and lies within the range of error for this study. Finally, the increase in SPL at large angles ($\varphi > 60$ deg) is due to the shock-associated acoustic waves, which are discussed above.

The results show that the actual overexpansion effects in acoustic far fields consist of shock-associated acoustic waves at high angles and a slight change in the peak angle of directivity. This also implies that the strength and directivity of the Mach wave source does not drastically change for each frequency range because far-field acoustic waves are strongly affected by the source strength and directivity but not by the source position.

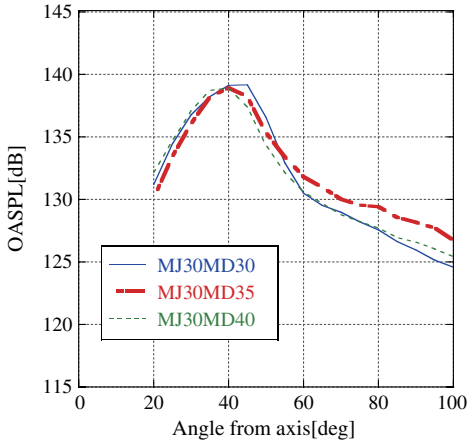

Fig. 12 Directivity at $R/D_J = 100$ for $M_J = 3.0$.

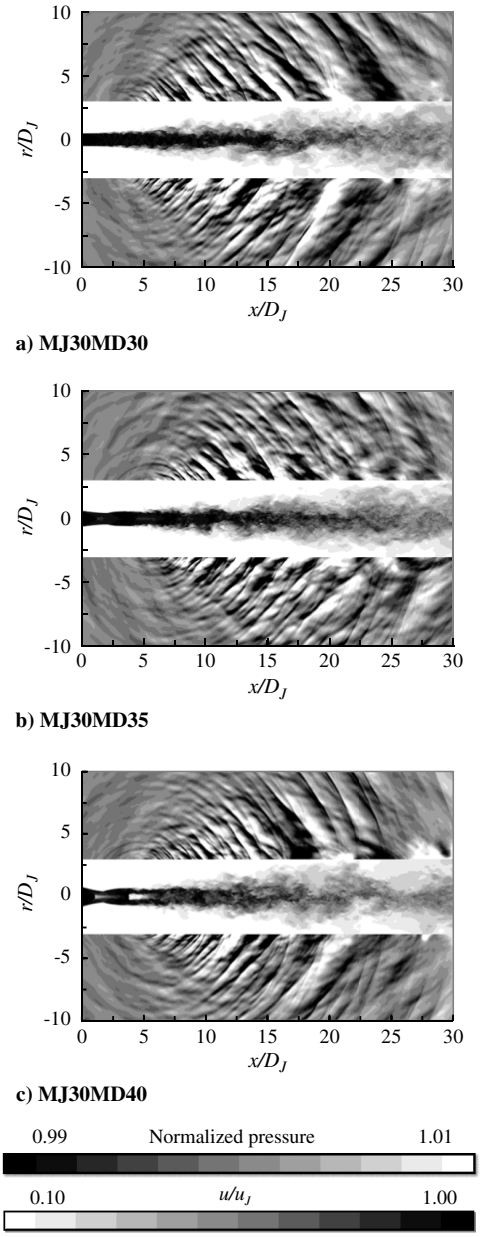

Fig. 13 Instantaneous flowfields for $M_J = 3.0$ jets. Center region shows velocity field, and outer region shows acoustic pressure field. For the velocity fields, contours are set from $0.1u_J$ to u_J. For pressure fluctuations, contours are set from $-0.01P_\infty$ to $0.01P_\infty$.

B. Actual Overexpansion Effects on Near Flow and Acoustic Field

1. Flowfields

The instantaneous flowfields of the three $M_J = 3.0$ jets are shown in Fig. 13. The strength of the Mach waves of these three jets is almost the same at the downstream region. This is due to the nondimensionalization based on the fully expanded parameters. If nondimensionalization based on design parameters was to be adopted, these plots would differ significantly from each other. Acoustic waves in the upstream region for the overexpanded jets MJ30MD35 and MJ30MD40 are slightly stronger than that for the ideally expanded jet MJ30MD30 because of the existence of shock-associated acoustic waves.

The average velocity fields of the three $M_J = 3.0$ jets are shown in Figs. 14 and 15. These figures are based on nondimensionalization using fully expanded parameters, and the obtained velocity distributions are again similar, while only slight changes can be found quantitatively. There are no strong shock waves in the case of MJ30MD30, while shock cells with/without Mach disks are observed in the cases of MJ30MD35 and MJ30MD40. When Mach disks are generated, clear slip lines are observed. These slip lines may cause enhancement in mixing of shear layer, as discussed later.

Figure 16 shows the velocity distributions along the axis. The velocity distributions are oscillatory in the overexpanded cases, while the ideally expanded cases do not have any oscillations. It is understood that the potential core length plays an important role in determining the source position of acoustic waves. Although it is difficult to determine the potential core length precisely from the available data of overexpanded jets because of the oscillation in the jet velocity, jet velocities in all cases appear to start to decrease at approximately $10 < x/D_J < 14$. There are approximately $2D_J$ to $4D_J$ differences for the position where the velocity starts to decrease. MJ30MD35 has an approximately $2D_J$ longer potential core length than MJ30MD30, and MJ30MD40 has an approximately $2D_J$ shorter potential core length than MJ30MD30, taking into consideration the difference in the position at $u/u_J = 0.8$ as depicted. Note that the position $u/u_J = 0.8$ does not directly indicate the potential core length. One of the causes of these discrepancies is the change in the position where shear-layer growth begins, as shown in the vorticity thickness of the shear layer shown in Fig. 17. Another cause of the differences between the jets is the change of the flowfield structure due to the existence of Mach disks in MJ30MD40.

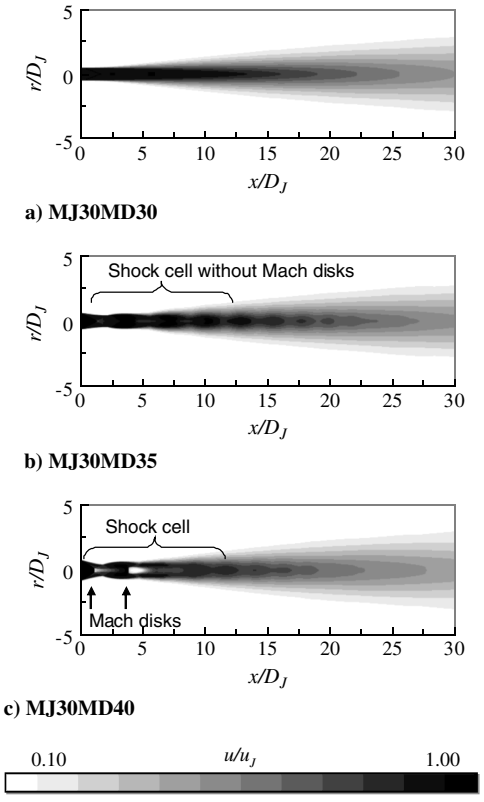

Fig. 14 Averaged velocity fields of $M_J = 3.0$ jets. Here, contours are set from $0.1U_J$ to U_J.

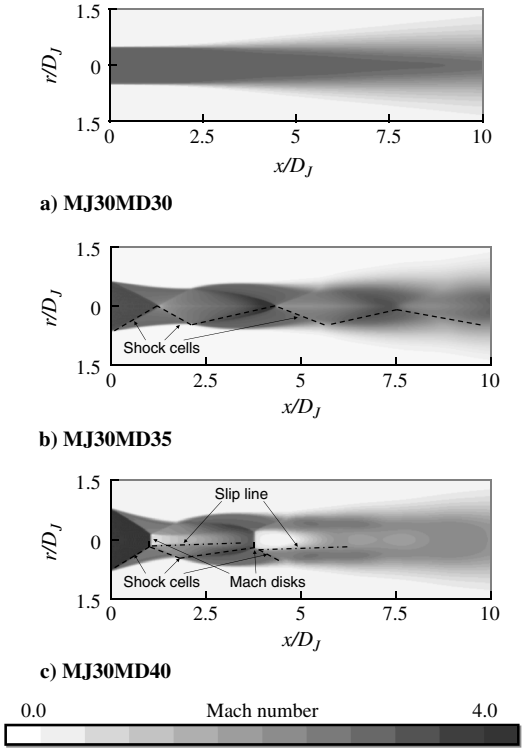

Fig. 15 Averaged Mach number distribution of near-nozzle region of $M_J = 3.0$ jets. Here, contours are set from 0.0 to 4.0. Also, flow structures are depicted in lower half of the figures.

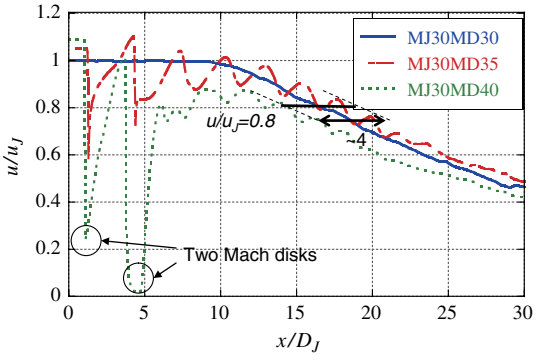

Fig. 16 Velocity distribution of $M_J = 3.0$ jets on axis.

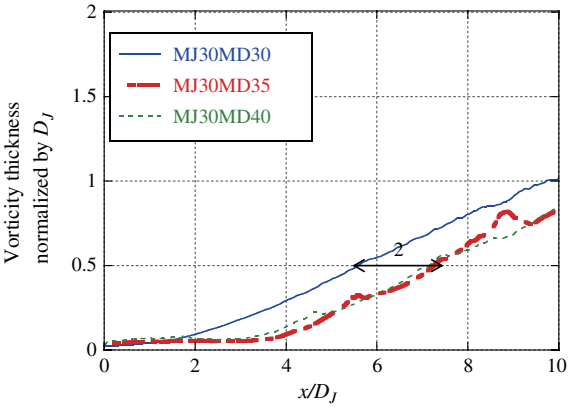

Fig. 17 Distribution of vorticity thickness of $M_J = 3.0$ jets.

The former effect can be observed in Fig. 17. The point where the shear-layer growth begins for the overexpanded jets (MJ30MD35 and MJ30MD40) is located at $x \sim 4D_J$, which is approximately $2D_J$ downstream compared with the ideally expanded jet. This position, where shear-layer growth begins for overexpanded jets, corresponds to the location of shock–shear-layer interactions, which are similar to the flowfields of an overexpanded jet computed by de Cacqueray et al. [48]. This effect on the position where shear-layer growth begins may be caused by two different physical and/or computational explanations. First, physical overexpansion effects (change in Mach number, density, or pressure at the near-nozzle region) affect the shear-layer instability. Second, the unresolved near-nozzle region changes the shear-layer development when the shear layer is not aligned with the grid lines for the overexpanded jets. It is difficult to determine which explanation is more dominant for the first effect (the change in the position of the shear-layer fluctuation) because the shear layer near the nozzle is extremely sensitive, as previously demonstrated for subsonic jets with a computational grid size of 200 million cells [49] and is beyond the scope of this paper. Instead, we are interested in the Mach wave generated by the large structure of turbulence observed further downstream. Thus, such a difference in the position where shear-layer growth begins is not considered in the remainder of our study. Meanwhile, an investigation of the reasons for the difference in shear-layer instability is a subject for future work.

In contrast, the effect of the Mach disks on the potential core length is a purely physical phenomenon. Mach disks generate high-speed and low-speed regions that promote the mixing of jets. This effect is discussed later with the velocity profile at the x constant plane.

As a result, the potential core length of MJ30MD35 becomes longer than that of MJ30MD30 because of the shear-layer instability

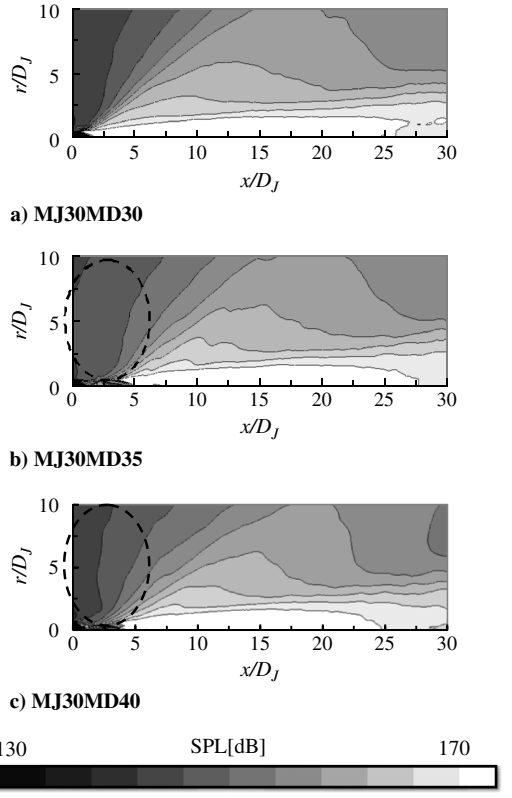

Fig. 19 OASPL distributions of $M_J = 3.0$ jets. Here, 11 contour lines are drawn between 130 and 170 dB.

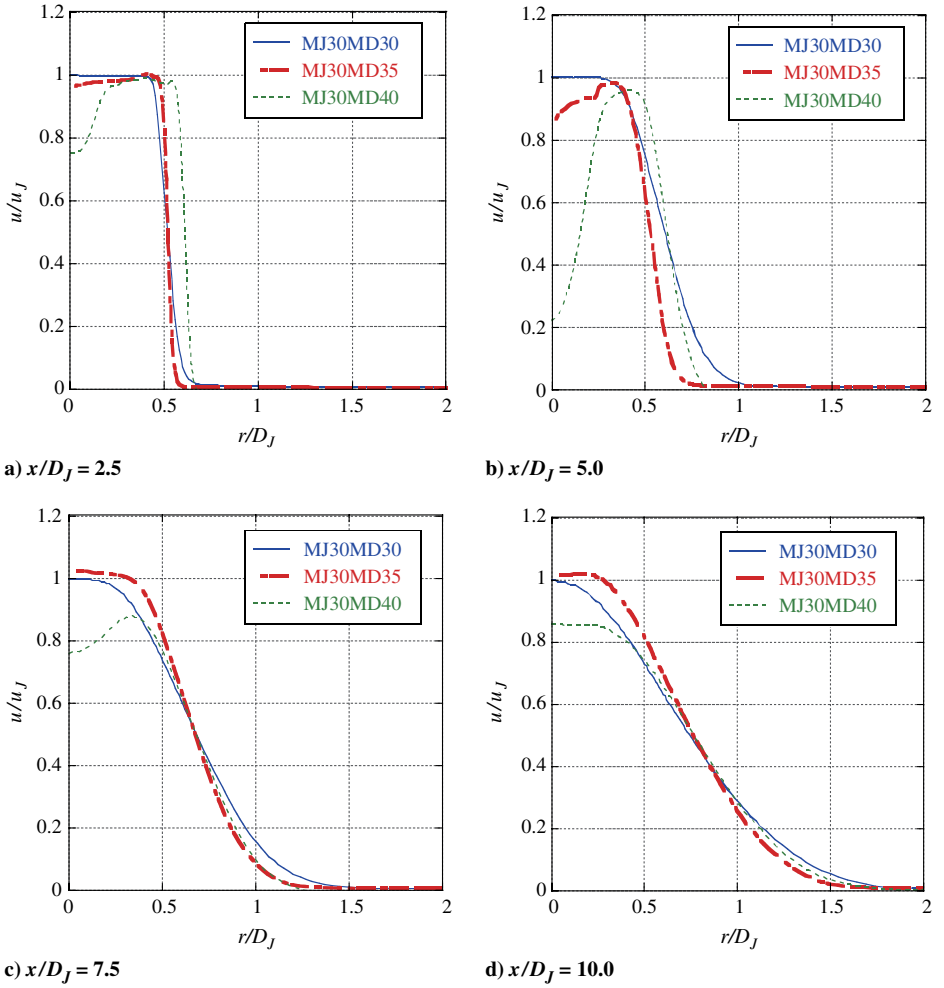

Fig. 18 Velocity profiles at constant x for $M_J = 3.0$ jets.

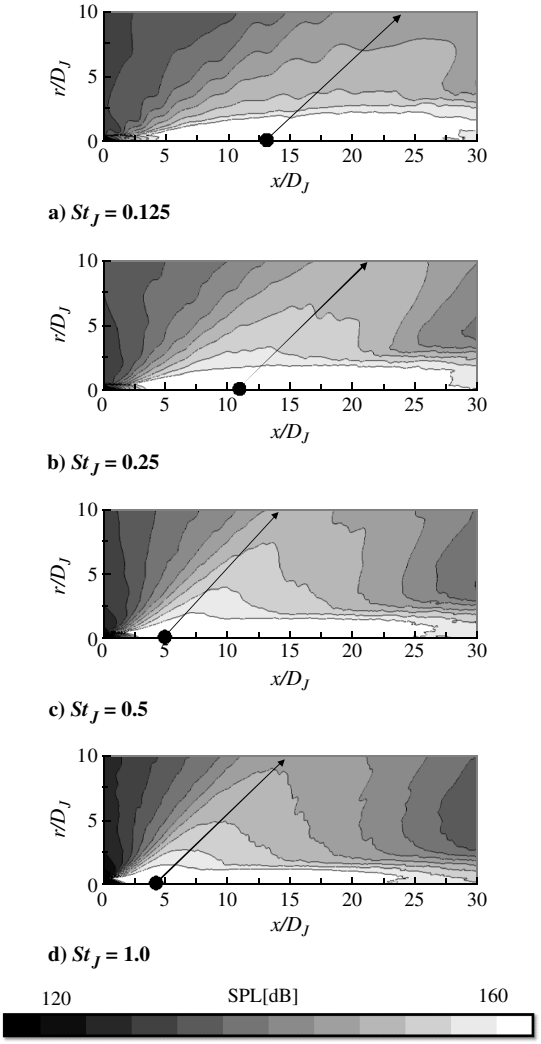

Fig. 20 OBSPL distributions for MJ30MD30. Here, 11 contour lines are drawn between 120 and 160 dB. Black dots show estimated source locations based on the microphone array method, and arrows show peak angles of acoustic wave emissions.

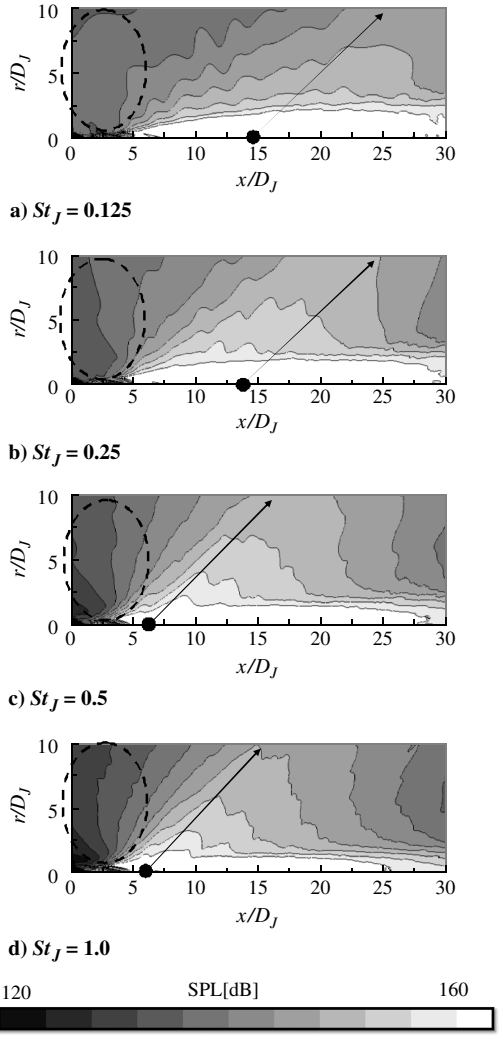

Fig. 21 OBSPL distributions for MJ30MD35. Here, 11 contour lines are drawn between 120 and 160 dB. Black dots show estimated source locations based on the microphone array method, and arrows show peak angles of acoustic wave emissions.

effect, as shown in Fig. 17. The potential core length of MJ30MD40 becomes shorter than that of MJ30MD30 because of the strong Mach disk effect, despite the fact that MJ30MD40 also includes the shear-layer instability effect as MJ30MD35 (Fig. 17).

The velocity profiles at different x positions are shown in Fig. 18. Because of the Mach disk generation in MJ30MD40, a low-speed region is observed at the center of the jet and a high-speed region surrounding the low-speed region is observed at $x/D_J = 2.5$, 5.0, and 7.5. The low-speed region and surrounding high-speed region enhances jet mixing, resulting in the early decay in the velocity near the center of the jet, as shown in the profile at $x/D_J = 10.0$, as compared with other jets. This enhancement of jet mixing corresponds to the early development of large-structure turbulence, which causes changes in source location in the case of MJ30MD40 as discussed later.

Conversely, comparing MJ30MD30 and MJ30MD35, MJ30MD35 has weaker oscillations at $x/D_J = 2.5$, 5.0, and 7.5, and its mixing is not enhanced as shown in the profile at $x/D_J = 10.0$. Therefore, shock cells without Mach disks do not have a strong effect on mixing.

2. *Near-Acoustic Fields*

The overall SPLs (OASPLs) of the three $M_J = 3.0$ jets are shown in Fig. 19. The data show that the intensity of the SPL contour lines does not change significantly. This is due to the nondimensionalization based on the fully expanded parameters, similar to what was found for the far-field sound pressure spectra. However, the shapes of the contour lines change for each case. This change is clearly observed in MJ30MD40 when compared with the other cases. This is due to the change in the source locations, because the strength and directivity of the acoustic wave sources do not significantly change based on the characteristics of the far-field acoustic field, as discussed earlier. Therefore, in the following discussion, we focus on the difference in source locations.

Comparing the OASPL for MJ30MD30 and MJ30MD35, the OASPL of MJ30MD35 is nearly identical to that of MJ30MD30, except that it is shifted downstream by approximately $2D_J$. Again, this is because of the difference in the position where shear-layer growth begins. Except for this effect, MJ30MD30 and MJ30MD35 have almost the same OASPL distributions.

The OASPL for MJ30MD40 displays a different SPL contour pattern. This is because the relative locations of sources of different frequencies change due to the Mach disks. This effect is discussed below using octave-band filtered SPL (OBSPL) distribution. Note that the SPL of an overexpanded jet in the upstream side (denoted by the dashed circles in Fig. 19) is higher than that of an ideally expanded jet. This is an effect of shock-associated acoustic waves.

The OBSPL distribution, source location (denoted by black dots), and angles of dominant acoustic wave emission (denoted by arrows) are shown in Figs. 20–22. Here, the source location is computed as the maximum point of source intensity obtained by using the microphone array method [50] (Appendix). The angles of dominant acoustic wave emission correspond to the maximum angle in the

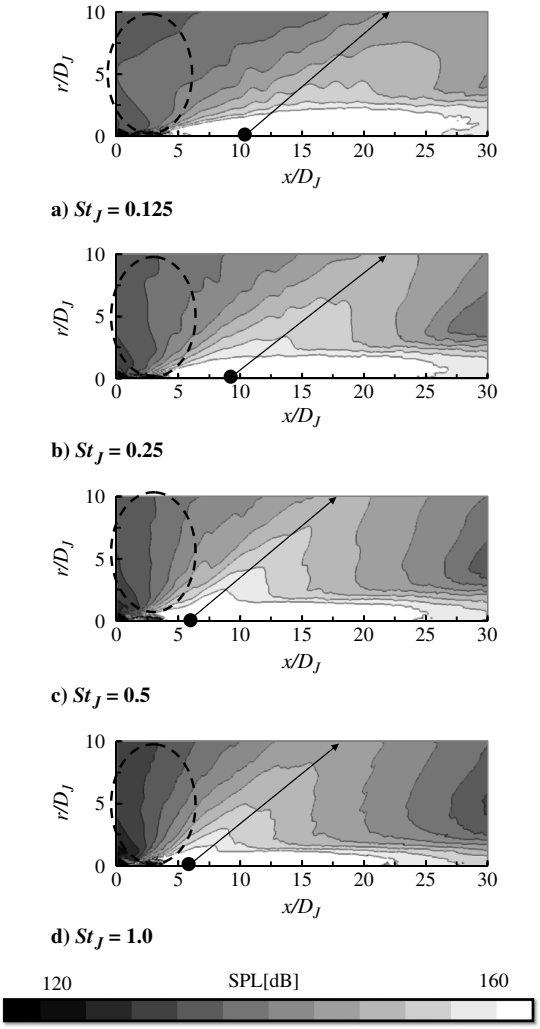

Fig. 22 OBSPL distributions of MJ30MD40. Here, 11 contour lines are drawn between 120 and 160 dB. Black dots show estimated source locations based on the microphone array method, and arrows show peak angles of acoustic wave emissions.

octave-band filtered far-field ($100D_J$) directivity with its origin located at the source location calculated using the microphone array method. This procedure (changing the origin of directivity) eliminates the error present in directivity because of the source position [51]. Figures 20–22 show that the sources of Mach waves move to the upstream with increasing Strouhal number. This characteristic is similar to that in a previous study by Nonomura [18].

A comparison of Figs. 20 and 21 shows that the SPL distribution of MJ30MD35 is nearly identical to that of MJ30MD30, except that it is shifted approximately $2D_J$ downstream. The source locations computed using the microphone array method (Fig. 23) show a similar trend for MJ30MD30 and MJ30MD35. The source location

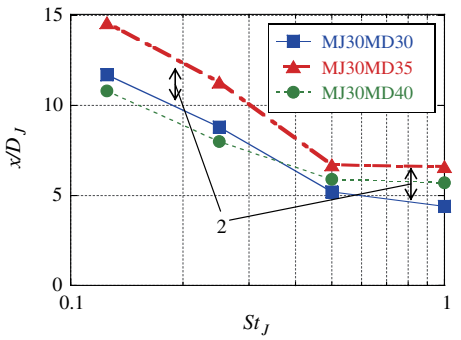

Fig. 23 Source locations computed by microphone array methods for $M_J = 3.0$ jets.

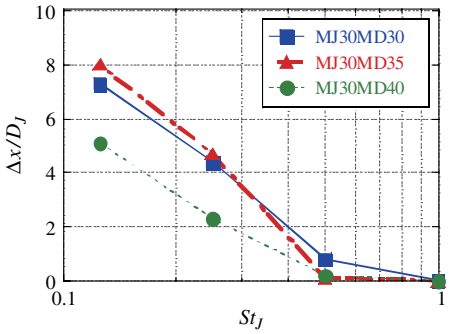

Fig. 24 Relative source locations based on high-frequency ($St = 1.0$) source location for $M_J = 3.0$ jets.

of MJ30MD35 is approximately $2D_J$ downstream to that of MJ30MD30 as depicted. This is because of the difference $\sim 2D_J$ in the position where the shear-layer fluctuation begins (Fig. 17).

For eliminating the change in the position where the shear-layer fluctuation begins, relative source locations based on the high-frequency source location are shown in Fig. 24. Here, we choose the high-frequency source location as point because it is directly affected by the position where the shear-layer fluctuation begins. Figure 24 illustrates that MJ30MD30 and MJ35MD35 have nearly identical relative source locations when the change in the position, where the shear-layer fluctuation begins, is eliminated. This result illustrates the Mach wave emission characteristics for overexpanded jets that have shock cells without Mach disks are nearly identical to the ideally expanded jet in each frequency range.

However, the low-frequency sources ($St = 0.125$, 0.25) for MJ30MD40 are located upstream compared with MJ30MD30. This can be seen in Fig. 23, or by comparing Figs. 20 and 22. On the other hand, the high-frequency sources ($St_J = 0.5$ and 1.0) are located further along the downstream side as compared with MJ30MD30 because of the change in position (where the shear-layer fluctuation begins) similar to MJ30MD35. If the effect of the change in the position where shear-layer fluctuations begin is eliminated, the low-frequency source position will appear to be located further along the upstream side, as shown in Fig. 24. This illustrates that when the shock-cell structure includes Mach disks, the source position moves further upstream. This is a very pronounced effect on the location of Mach wave sources for overexpanded supersonic jets. This effect can be explained by the enhancement of mixing discussed in Fig. 18, which leads to the early development of large structure of turbulence in the upstream.

VI. Conclusions

To predict the acoustic waves emitted from a rocket plume, overexpansion effects on Mach waves from $M_J = 3.0$ supersonic jets were investigated in this study. Nondimensionalization based on fully expanded parameters was verified, and actual overexpansion effects under the nondimensionalization were discussed using computational results of ideally expanded and overexpanded jets. The results of acoustic far fields show that the nondimensionalization based on ideally expanded parameters works well, similar to the results for low-Mach-number underexpanded jets in previous studies. Thus, a close correspondence is seen in the plot of SPL spectra, except for the existence of shock-associated acoustic waves observed at 90 deg. These results illustrate that the nondimensionalization improves the accuracy of subsequent predictions of acoustic waves from rocket plumes because one parameter M_D can be neglected for acoustic far fields. Comparisons of the flowfields and near-acoustic fields under the nondimensionalization show that Mach wave sources move approximately twice the nozzle diameter upstream due to the existence of Mach disks. This is because the low-speed region generated by the Mach disk enhances shear-layer mixing. This also illustrates that the source position may be changed by the existence of Mach disks and that it is necessary to take special care for jets with Mach disks. Furthermore, the overexpanded jet,

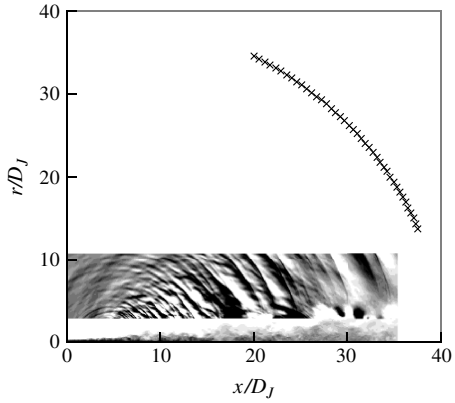

Fig. A1 Microphone array positions.

which has a shock cell without Mach disks, exhibits the same Mach wave generation characteristics as the ideally expanded jet under the nondimensionalization. For the prediction of acoustic waves from overexpanded jets without Mach disks, conjecture based on the data of an ideally expanded jet will be useful.

Appendix

In this Appendix, the identification of source locations by using the microphone array method adopted in Sec. V is briefly described. This methodology is similar to the one adopted in [50].

First, the time-series sound pressure fluctuations at the microphone positions are computed by the time-domain Kirchhoff method. Here, 21 microphones in 12 azimuthal planes (a total of 252 microphone positions) are located at $R = 40D_J$ from the center of the nozzle. The angle from the axis is set in between 20 and 40 deg in 1 deg intervals. The microphone positions in one azimuthal plane are shown in Fig. A1.

The time-series sound pressure is transformed into azimuthal Fourier modes. In this study, the zeroth mode (azimuthal average) acoustic radiation is only considered because the lower azimuthal modes are dominant for jet acoustics [50]. Furthermore, segments of time-series azimuthal modes are transformed into frequency domain Fourier modes by using a short-time Fourier transform. Here, the window width is set to the length of four time periods, and a Hanning window is employed. Segments of time-series data are also overlapped, and the number of frequency domain Fourier modes increases for averaging the correlation matrix. Based on these Fourier modes, a correlation matrix of signals at the microphone positions is computed and averaged. The intensities of source locations on the axis are computed using the correlation matrix [52].

Finally, the position where the maximum intensity is observed is selected as the source location for each frequency.

Acknowledgments

The authors gratefully acknowledge S. Tsutsumi, K. Fukuda, and A. Oyama for their comments on this paper. The authors are also grateful to the reviewers for their constructive comments.

References

[1] Eldred, K. M., "Acoustic Loads Generated by Propulsion System," NASA, SP 8072, 1971.

[2] Varnier, J., "Experimental Study and Simulation of Rocket Engine Freejet Noise," *AIAA Journal*, Vol. 39, No. 10, 2001, pp. 1851–1859. doi:10.2514/2.1199

[3] Tsutsumi, S., Shima, E., Takaki, R., and Fujii, K., "Generation and Propagation of Pressure Waves from H-IIA Launch Vehicle at Lift-Off," AIAA Paper 2008-0390, 2008.

[4] Tsutsumi, S., Fukuda, K., Takaki, R., Shima, E., Fujii, K., and Ui, K., "Numerical Study on Acoustic Radiation for Designing Launch-Pad of Advanced Solid Rocket," AIAA Paper 2008-5148, 2008.

[5] Tsutsumi, S., Kato, S., Fukuda, K., Takaki, R., and Ui, K., "Effect of Deflector Shape on Acoustic Field of Launch Vehicle at Lift-Off," AIAA Paper 2009-0328, 2009.

[6] Bailly, C., and Bogey, C., "Contributions of Computational Aeracoustics to Jet Noise Research and Prediction," *International Journal of Computational Fluid Dynamics*, Vol. 18, No. 6, 2004, pp. 481–491. doi:10.1080/10618560410001673498

[7] Bodony, D., and Lele, S., "Current Status of Jet Noise Predictions Using Large-Eddy Simulation," *AIAA Journal*, Vol. 46, No. 2, 2008, pp. 364–380. doi:10.2514/1.24475

[8] Kim, C., Krejsa, E., and Khavaran, A., "Significance of Shock Structure on Supersonic Jet Mixing Noise of Axisymmetric Nozzles," *AIAA Journal*, Vol. 32, No. 9, 1994, pp. 1920–1923. doi:10.2514/3.12192

[9] Tam, C. K., "Dimensional Analysis of Jet Noise Data," AIAA Paper 2005-2938, 2005.

[10] Tam, C. K., Golebiowski, M., and Seiner, J. M., "On the Two Components of Turbulent Mixing Noise from Supersonic Jets," AIAA Paper 1996-1716, 1996.

[11] Tam, C. K. W., and Tanna, H., "Shock Associated Noise of Supersonic Jet from Convergent Divergent Nozzle," *Journal of Sound and Vibration*, Vol. 81, No. 3, 1982, pp. 337–358. doi:10.1016/0022-460X(82)90244-9

[12] Tam, C. W. K., "Supersonic Jet Noise," *Annual Review of Fluid Mechanics*, Vol. 27, 1995, pp. 17–43. doi:10.1146/annurev.fl.27.010195.000313

[13] Petitjean, B., Morris, P., and McLaughlin, D., "On the Nonlinear Propagation of Shock-Associated Jet Noise," AIAA Paper 2005-2930, 2005, pp. 1–15.

[14] Viswanathan, K., Alkislar, M., and Czech, M., "Characteristics of the Shock Noise Component of Jet Noise," *AIAA Journal*, Vol. 48, No. 1, 2010, pp. 25–46. doi:10.2514/1.38521

[15] Yüceil, K. B., and Ötügen, M. V., "Scaling Parameters for Underexpanded Supersonic Jets," *Physics of Fluids*, Vol. 14, No. 12, 2002, pp. 4206–4215. doi:10.1063/1.1513796

[16] Inman, J. A., Danehy, P. M., Nowak, R. J., and Alderfer, D. W., "Identification of Instability Modes of Transition in Underexpanded Jets," AIAA Paper 2008-4389, 2008.

[17] Anderson, J. D., *Modern Compressible Flow*, McGraw–Hill, New York, 1982, pp. 154–156.

[18] Nonomura, T., "Characteristics of Acoustic Waves Generated by Flow Instability of Supersonic Jets," Ph.D. Thesis, Univ. of Tokyo, Tokyo, 2008.

[19] Fukuda, Y., Teramotoand, S., and Nagashima, T., "Large Eddy Simulation of a High Subsonic Jet and Noise Generation," *Proceedings of Asian Joint Conference on Propulsion and Power 2008, C7-2*, Japan Soc. for Aeronautical and Space Sciences Paper C7-2, Tokyo, 2008.

[20] Bogey, C., and Bailly, C., "LES of a High Reynolds, High Subsonic Jet: Effect of the Inflow Conditions on Flow and Noise," AIAA Paper 2003-3170, 2003.

[21] Sandham, N., and Reynolds, W., "Compressible Mixing Layer: Linear Theory and Direct Simulation," *AIAA Journal*, Vol. 28, No. 4, 1990, pp. 618–624. doi:10.2514/3.10437

[22] Sandham, N., and Reynolds, W., "Three-Dimensional Simulations of Large Eddies in the Compressible Mixing Layer," *Journal of Fluid Mechanics*, Vol. 224, 1991, pp. 133–158. doi:10.1017/S0022112091001684

[23] Jiang, G.-S., and Shu, C.-W., "Efficient Implementation of Weighted ENO Schemes," *Journal of Computational Physics*, Vol. 126, No. 1, 1996, pp. 202–228. doi:10.1006/jcph.1996.0130

[24] Lele, S. K., "Compact Finite Difference Schemes with Spectral-Like Resolution," *Journal of Computational Physics*, Vol. 103, No. 1, 1992, pp. 16–42. doi:10.1016/0021-9991(92)90324-R

[25] Deng, X. G., and Zhang, H., "Developing High-Order Weighted Compact Nonlinear Schemes," *Journal of Computational Physics*, Vol. 165, No. 1, 2000, pp. 22–44. doi:10.1006/jcph.2000.6594

[26] Zhang, S., Jiang, S., and Shu, C.-W., "Development of Nonlinear Weighted Compact Schemes with Increasingly Higher Order Accuracy," *Journal of Computational Physics*, Vol. 227, 2008, pp. 7294–7321. doi:10.1016/j.jcp.2008.04.012

[27] Nonomura, T., Iizuka, N., and Fujii, K., "Freestream and Vortex Preservation Properties of High-Order WENO and WCNS on

Curvilinear Grids," *Computers and Fluids*, Vol. 39, No. 2, 2010, pp. 197–214. doi:10.1016/j.compfluid.2009.08.005

[28] Deng, X., Mao, M., Tu, G., Liu, H., and Zhang, H., "Geometric Conservation Law and Applications to High-Order Finite Difference Schemes with Stationary Grids," *Journal of Computational Physics*, Vol. 230, No. 4, 2011, pp. 1100–1115. doi:10.1016/j.jcp.2010.10.028

[29] Nonomura, T., Iizuka, N., and Fujii, K., "Increasing Order of Accuracy of Weighted Compact Nonlinear Scheme," AIAA Paper 2007-0893, 2007.

[30] Nonomura, T., and Fujii, K., "Effects of Difference Scheme Type in High-Order Weighted Compact Nonlinear Schemes," *Journal of Computational Physics*, Vol. 228, 2009, pp. 3533–3539. doi:10.1016/j.jcp.2009.02.018

[31] Taylor, G., Kroker, A., and Gursul, I., "Passive Flow Control over Flexible Non-Slender Delta Wings," AIAA Paper 2005-0865, 2005.

[32] Nonomura, T., Goto, Y., Li, W., and Fujii, K., "Efficiency Improvements of Seventh-Order Weighted Compact Nonlinear Scheme," *Computational Fluid Dynamics Journal*, Vol. 18, 2011, pp. 180–186.

[33] Shima, E., and Jounouchi, T., "Role of CFD in Aeronautical Engineering (No. 14) AUSM Type Upwind Schemes," *Proceedings of the 14th NAL Symposium on Aircraft Computational Aerodynamics*, National Aerospace Lab. of Japan, Tokyo, 1997, pp. 7–12.

[34] Liou, M. S., and Steffen, C., Jr., "A New Flux Splitting Scheme," *Journal of Computational Physics*, Vol. 107, 1993, pp. 23–39. doi:10.1006/jcph.1993.1122

[35] Boris, J. P., Grinstein, F. F., Oran, E., and Kolbe, R. J., "New Insights into Large Eddy Simulation," *Fluid Dynamics Research*, Vol. 10, 1992, pp. 199–228. doi:10.1016/0169-5983(92)90023-P

[36] Ishiko, K., "Study of Implicit LES for Compressible Turbulent Flows Using Weighted Compact Nonlinear Scheme," Ph.D. Thesis, Tohoku Univ., Sendai, Japan, 2009.

[37] Ishiko, K., Ohnishi, N., Ueno, K., and Sawada, K., "Implicit Large Eddy Simulation of Two-Dimensional Homogeneous Turbulence Using Weighted Compact Nonlinear Scheme," *Journal of Fluids Engineering*, Vol. 131, No. 6, 2009, Paper 061401. doi:10.1115/1.3077141

[38] Gottlieb, S., and Shu, C.-W., "Total Variation Diminishing Runge–Kutta Schemes," *Mathematics of Computation*, Vol. 67, No. 221, 1998, pp. 73–85, 221. doi:10.1090/S0025-5718-98-00913-2

[39] Colonius, T., Lele, S. K., and Moin, P., "Boundary Condition for Direct Computation of Aerodynamics Sound Generation," *AIAA Journal*, Vol. 31, No. 9, 1993, pp. 1574–1582. doi:10.2514/3.11817

[40] Pan, F., Uzun, A., and Lyrintzis, A. S., "Refraction Corrections for Surface Integral Methods in Jet Aeroacoustics," AIAA Paper 2004-2873, 2004.

[41] Lau, J. C., Morris, P. J., and Fisher, M. J., "Measurements in Subsonic and Supersonic Jets Using a Laser Velocimeter," *Journal of Fluid Mechanics*, Vol. 93, 1979, pp. 1–27. doi:10.1017/S0022112079001750

[42] Seiner, J. M., and Ponton, M. K., "Aeroacoustic Data for High Reynolds Number Supersonic Axisymmetric Jets," NASA, TM 86296, 1985.

[43] Troutt, T. R., and McLaughlin, D. K., "Experiments on the Flow and Acoustic Properties of a Moderate-Reynolds-Number Supersonic Jet," *Journal of Fluid Mechanics*, Vol. 116, 1982, pp. 123–156. doi:10.1017/S0022112082000408

[44] Tanna, H., "An Experimental Study of Jet Noise Part I: Turbulent Mixing Noise," *Journal of Sound and Vibration*, Vol. 50, No. 3, 1977, pp. 405–428. doi:10.1016/0022-460X(77)90493-X

[45] Tam, C. K. W., Seiner, J. M., and Yu, J., "Proposed Relationship between Broadband Shock Associated Noise and Screech Tones," *Journal of Sound and Vibration*, Vol. 110, No. 2, 1986, pp. 309–321. doi:10.1016/S0022-460X(86)80212-7

[46] Norum, T. D., and Seiner, J. M., "Location and Propagation of Shock Associated Noise from Supersonic Jets," AIAA Paper 1980-0983, 1980.

[47] Tam, C., "Mach Wave Radiation from High-Speed Jets," AIAA Paper 2009-13, 2009.

[48] de Cacqueray, N., Bogey, C., and Bailly, C., "Direct Noise Computation of a Shocked and Heated Jet at a Mach Number of 3.30," AIAA Paper 2010-3732, 2010.

[49] Bogey, C., Marsden, O., and Bailly, C., "Flow and Acoustic Fields of Reynolds Number 105, Subsonic Jets with Tripped Exit Boundary Layers," AIAA Paper 2010-3727, 2010.

[50] Suzuki, T., Bodony, D., Ryu, J., and Lele, S. K., "Noise Sources of High-Mach-Number Jets at Low Frequencies Studied with a Phased-Array Approach Based on LES Database," *Center for Turbulence Research Annual Research Briefs 2007* [online], 2007, pp. 287–301, http://ctr.stanford.edu/ResBriefs07/25_takao_pp287_302.pdf [retrieved 2011].

[51] Kuo, C.-W., Veltin, J., and McLaughlin, D. K., "Effects of Jet Noise Source Distribution on Acoustic Far-Field Measurements," AIAA Paper 2010-474, 2010.

[52] Mosher, M., "Phased Arrays for Aeroacoustic Testing: Theoretical Development," AIAA Paper 1996-1713, 1996.

C. Bailly
Associate Editor